

TriDoNet: A Triple Domain Model-driven Network for CT Metal Artifact Reduction

Baoshun Shi, Ke Jiang, Shaolei Zhang, Qiusheng Lian, and Yanwei Qin

Abstract—Recent deep learning-based methods have achieved promising performance for computed tomography metal artifact reduction (CTMAR). However, most of them suffer from two limitations: (i) the domain knowledge is not fully embedded into the network training; (ii) metal artifacts lack effective representation models. The aforementioned limitations leave room for further performance improvement. Against these issues, we propose a novel triple domain model-driven CTMAR network, termed as TriDoNet, whose network training exploits triple domain knowledge, i.e., the knowledge of the sinogram, CT image, and metal artifact domains. Specifically, to explore the non-local repetitive streaking patterns of metal artifacts, we encode them as an explicit tight frame sparse representation model with adaptive thresholds. Furthermore, we design a contrastive regularization (CR) built upon contrastive learning to exploit clean CT images and metal-affected images as positive and negative samples, respectively. Experimental results show that our TriDoNet can generate superior artifact-reduced CT images.

Index Terms—Metal artifact reduction, model-driven network, tight frame, triple domain network.

I. INTRODUCTION

COMPUTED tomography (CT) has become essential for clinical diagnosis and treatment plans. However, due to the metallic implants within patients, X-ray projections are incomplete, causing severe non-local streaking and star-shape artifacts in CT images [1]–[3]. Reducing these structured and non-local metal artifacts is a critical problem in the field of CT [4]. The early attempts to address this problem were the sinogram completion and iterative metal artifact reduction (MAR) algorithms. However, sinogram completion methods, such as linear interpolation (LI) [5] and normalized MAR (NMAR) [6], usually lead to secondary artifacts in restored CT images. Moreover, iterative MAR algorithms require hand-crafted regularizers, and their iteration processes are time-consuming [7].

Recently, MAR methods based on deep learning have achieved promising performance. According to different

domain knowledge, the existing deep learning-based MAR methods can be categorized into three classes: sinogram domain networks, image domain networks, and dual domain networks. Among them, sinogram domain networks correct metal-affected sinograms and then restore CT images by filtered back projection (FBP), which inevitably produces new artifacts [8], [9]. Image domain methods regard the MAR task as an image restoration task and design the MAR networks based on image domain knowledge but ignore sinogram domain knowledge [10], [11]. More recent methods address this issue by embedding dual domain knowledge, such as [12]–[16]. Although current state-of-the-art (SOTA) dual domain networks have achieved high-quality CT images, less domain knowledge utilized for training and lacking effective representation models of metal artifacts are two main limitations, leaving room for further performance improvement. To mitigate these gaps, we propose a novel triple domain model-driven network. Our main contributions and innovations are summarized as follows.

- We propose the so-called TriDoNet, a triple domain unfolding network for MAR. TriDoNet ensures information interaction between the sinogram, CT image, and metal artifact domains in order to help them promote and complement each other. More precisely, we first formulate a triple domain optimization model and then solve it with an alternating iterative algorithm. The iterative steps of the algorithm are unfolded into corresponding network modules, thus the network architecture inherits the interpretability of iterative algorithms.

- We propose a supervised tight frame learning method in the metal artifact domain to represent the delicate structures of metal artifacts. A deep threshold network (DTN) is elaborated to determine spatial-varied thresholds. The learned tight frame with adaptive thresholds can capture the structure information of metal artifacts. Ablation experiments have demonstrated that the metal artifact domain sub-network using tight frame and DTN could achieve better results.

- We propose a contrastive regularization (CR) to further improve the performance of MAR networks. CR can ensure that restored CT images are pulled closer to clean CT images and pushed far away from metal-affected CT images in the representation space. Experimental results demonstrate the superior performance of TriDoNet compared with SOTA MAR methods, such as ACDNet [16] and InDuDoNet [3].

This work was supported by the National Natural Science Foundation of China under Grants 61901406, 61871275, 61827809, 62271330, and 61971292, by the Natural Science Foundation of Hebei Province under Grant F2020203025 and F2022203030, by the Young Talent Program of Universities and Colleges in Hebei Province under Grant BJ2021044, and by the Hebei Key Laboratory Project under Grant 202250701010046.

B. S. Shi (Corresponding author), K. Jiang, S. L. Zhang, and Q. S. Lian are with the School of Information Science and Engineering, Yanshan University, Qinhuang Dao 066004, China. (E-mail: shibaoshun@ysu.edu.cn).

Y. W. Qin is with the School of Mathematical Sciences, Capital Normal University, Beijing 100048, China.

II. THE PROPOSED METHODS

A. Triple domain model-driven network

For an observed metal-affected CT image \mathbf{y} , it consists of two regions, namely metal region and non-metal region [17]. In this paper, we focus on the non-metal region. Mathematically, the decomposition model can be expressed as

$$\mathbf{m} \odot \mathbf{y} = \mathbf{m} \odot \mathbf{x} + \mathbf{m} \odot \mathbf{e} \quad (1)$$

where \mathbf{m} is the binary non-metal mask, \mathbf{x} is the artifact-free CT image, \mathbf{e} is the metal artifact, and \odot is an element-wise product.

Generally, the normalized metal-affected sinogram is homogeneous [3]. Therefore, we correct the normalized one. Formally, the sinogram s can be written as

$$s = \tilde{z} \odot \tilde{s} \quad (2)$$

where \tilde{z} is the normalization coefficient obtained from the prior sinogram, and \tilde{s} is the normalized sinogram.

To explore triple domain knowledge, i.e., the knowledge of the sinogram, CT image, and metal artifact domains, a possible triple domain MAR optimization problem is formulated as

$$\begin{aligned} \min_{\tilde{s}, \mathbf{e}, \mathbf{x}} & \|\mathbf{m} \odot (\mathbf{y} - \mathbf{x} - \mathbf{e})\|_2^2 + \alpha \|\mathbf{P}\mathbf{x} - \tilde{z} \odot \tilde{s}\|_2^2 \\ & + \beta \|(1 - \mathbf{tr}) \odot (\tilde{z} \odot \tilde{s} - \mathbf{s}_{ma})\|_2^2 \\ & + \gamma_1 R_1(\tilde{s}) + \gamma_2 R_2(\mathbf{e}) + \gamma_3 R_3(\mathbf{x}) \end{aligned} \quad (3)$$

where \mathbf{tr} is the binary metal trace, \mathbf{P} is the Radon transform, i.e., forward projection (FP), and \mathbf{s}_{ma} is the metal-affected sinogram. In Eqn. (3), $R_1(\bullet)$, $R_2(\bullet)$, and $R_3(\bullet)$ are regularization functions that impose some desirable properties onto \tilde{s} , \mathbf{e} , and \mathbf{x} , respectively. Moreover, α , β , γ_1 , γ_2 , and γ_3 are weight factors.

We explore the sparsity of metal artifacts over the learned tight frame $\mathbf{W} \in \mathbb{R}^{M \times N}$ ($M \geq N$) to formulate the regularizer of metal artifacts, i.e., $R_2(\mathbf{e}) = \|\mathbf{W}\mathbf{e}\|_1$. Here, $\|\bullet\|_1$ represents the l_1 norm. The triple domain reconstruction problem defined in Eqn. (3) can be recast as

$$\begin{aligned} \min_{\tilde{s}, \mathbf{e}, \mathbf{x}} & \|\mathbf{m} \odot (\mathbf{y} - \mathbf{x} - \mathbf{e})\|_2^2 + \alpha \|\mathbf{P}\mathbf{x} - \tilde{z} \odot \tilde{s}\|_2^2 \\ & + \beta \|(1 - \mathbf{tr}) \odot (\tilde{z} \odot \tilde{s} - \mathbf{s}_{ma})\|_2^2 \\ & + \gamma_1 R_1(\tilde{s}) + \gamma_2 \|\mathbf{W}\mathbf{e}\|_1 + \gamma_3 R_3(\mathbf{x}). \end{aligned} \quad (4)$$

We exploit an alternating iteration method to solve the triple domain MAR optimization problem defined in Eqn. (4), and proximal operators are utilized to solve each sub-problem. At the $(t+1)$ -th iteration, \tilde{s} , \mathbf{e} , and \mathbf{x} are alternately updated as follows.

Updating \tilde{s} : Given $\mathbf{e}^{(t)}$ and $\mathbf{x}^{(t)}$, the sub-problem of updating \tilde{s} is derived as

$$\begin{aligned} \min_{\tilde{s}} & \alpha \|\mathbf{P}\mathbf{x}^{(t)} - \tilde{z} \odot \tilde{s}\|_2^2 \\ & + \beta \|(1 - \mathbf{tr}) \odot (\tilde{z} \odot \tilde{s} - \mathbf{s}_{ma})\|_2^2 + \gamma_1 R_1(\tilde{s}). \end{aligned} \quad (5)$$

The quadratic approximation of the sub-problem defined in Eqn. (5) is

$$\begin{aligned} \min_{\tilde{s}} & g_1(\tilde{s}^{(t)}) + \langle \tilde{s} - \tilde{s}^{(t)}, \nabla g_1(\tilde{s}) \rangle \\ & + \frac{1}{2\eta_1} \|\tilde{s} - \tilde{s}^{(t)}\|_2^2 + \gamma_1 R_1(\tilde{s}) \end{aligned} \quad (6)$$

where $g_1(\tilde{s}^{(t)}) = \alpha \|\mathbf{P}\mathbf{x}^{(t)} - \tilde{z} \odot \tilde{s}^{(t)}\|_2^2 + \beta \|(1 - \mathbf{tr}) \odot (\tilde{z} \odot \tilde{s}^{(t)} - \mathbf{s}_{ma})\|_2^2$, and η_1 is the stepsize. Equation (6) can be equivalently written as

$$\min_{\tilde{s}} \frac{1}{2} \|\tilde{s} - (\tilde{s}^{(t)} - \eta_1 \nabla g_1(\tilde{s}^{(t)}))\|_2^2 + \gamma_1 \eta_1 R_1(\tilde{s}) \quad (7)$$

where $\nabla g_1(\tilde{s}^{(t)}) = \alpha \tilde{z} \odot (\tilde{z} \odot \tilde{s}^{(t)} - \mathbf{P}\mathbf{x}^{(t)}) + \beta(1 - \mathbf{tr}) \odot \tilde{z} \odot (\tilde{z} \odot \tilde{s}^{(t)} - \mathbf{s}_{ma})$. Using the proximal gradient algorithm, the update rule of \tilde{s} can be described as

$$\tilde{s}^{(t+1)} \triangleq \text{prox}_{\gamma_1 \eta_1 R_1}(\tilde{s}^{(t+0.5)}). \quad (8)$$

where $\text{prox}_{\gamma_1 \eta_1 R_1}(\bullet)$ is a proximal operator related to $R_1(\bullet)$. Given $\tilde{s}^{(t+0.5)} = \tilde{s}^{(t)} - \eta_1 \nabla g_1(\tilde{s}^{(t)})$, we have

$$\begin{aligned} \tilde{s}^{(t+0.5)} & = \tilde{s}^{(t)} - \eta_1 \alpha \tilde{z} \odot (\tilde{z} \odot \tilde{s}^{(t)} - \mathbf{P}\mathbf{x}^{(t)}) \\ & - \eta_1 \beta (1 - \mathbf{tr}) \odot \tilde{z} \odot (\tilde{z} \odot \tilde{s}^{(t)} - \mathbf{s}_{ma}). \end{aligned} \quad (9)$$

Updating \mathbf{e} : Fix $\tilde{s}^{(t+1)}$ and $\mathbf{x}^{(t)}$, we can update \mathbf{e} by solving the following sub-problem

$$\min_{\mathbf{e}} \|\mathbf{m} \odot (\mathbf{y} - \mathbf{x}^{(t)} - \mathbf{e})\|_2^2 + \gamma_2 \|\mathbf{W}\mathbf{e}\|_1. \quad (10)$$

Similarly, the updating rule of \mathbf{e} is written as

$$\mathbf{e}^{(t+1)} \triangleq \text{prox}_{\gamma_2 \eta_2 R_2}(\mathbf{e}^{(t+0.5)}) \quad (11)$$

where

$$\mathbf{e}^{(t+0.5)} = (1 - \eta_2 \mathbf{m}) \odot \mathbf{e}^{(t)} + \eta_2 \mathbf{m} \odot (\mathbf{y} - \mathbf{x}^{(t)}). \quad (12)$$

The tight frame \mathbf{W} satisfies tight property $\|\mathbf{W}\mathbf{e}\|_2^2 = \|\mathbf{e}\|_2^2$, thus Eqn. (11) can be expressed as

$$\mathbf{e}^{(t+1)} = \mathbf{W}^T \text{soft}(\mathbf{W}\mathbf{e}^{(t+0.5)}, \varepsilon) \quad (13)$$

where $\text{soft}(u, \varepsilon) = \text{sign}(u) \max(|u| - \varepsilon, 0)$ is the soft threshold function, and $\varepsilon = \gamma_2 \eta_2$ is the threshold. In this paper, we utilize an elaborated DTN to adaptively determine the thresholds from the coefficients of metal artifacts, i.e., $\varepsilon = f(\mathbf{W}\mathbf{e}^{(t+0.5)})$. Here, $f(\bullet)$ is the so-called DTN, whose network architecture is described in Sec. II-B.

Updating \mathbf{x} : Given $\tilde{s}^{(t+1)}$ and $\mathbf{e}^{(t+1)}$, \mathbf{x} is updated by solving the following sub-problem

$$\begin{aligned} \min_{\mathbf{x}} & \|\mathbf{m} \odot (\mathbf{y} - \mathbf{x} - \mathbf{e}^{(t+1)})\|_2^2 \\ & + \alpha \|\mathbf{P}\mathbf{x} - \tilde{z} \odot \tilde{s}^{(t+1)}\|_2^2 + \gamma_3 R_3(\mathbf{x}). \end{aligned} \quad (14)$$

Similarly, the updating rule of \mathbf{x} is written as

$$\mathbf{x}^{(t+1)} \triangleq \text{prox}_{\gamma_3 \eta_3 R_3}(\mathbf{x}^{(t+0.5)}) \quad (15)$$

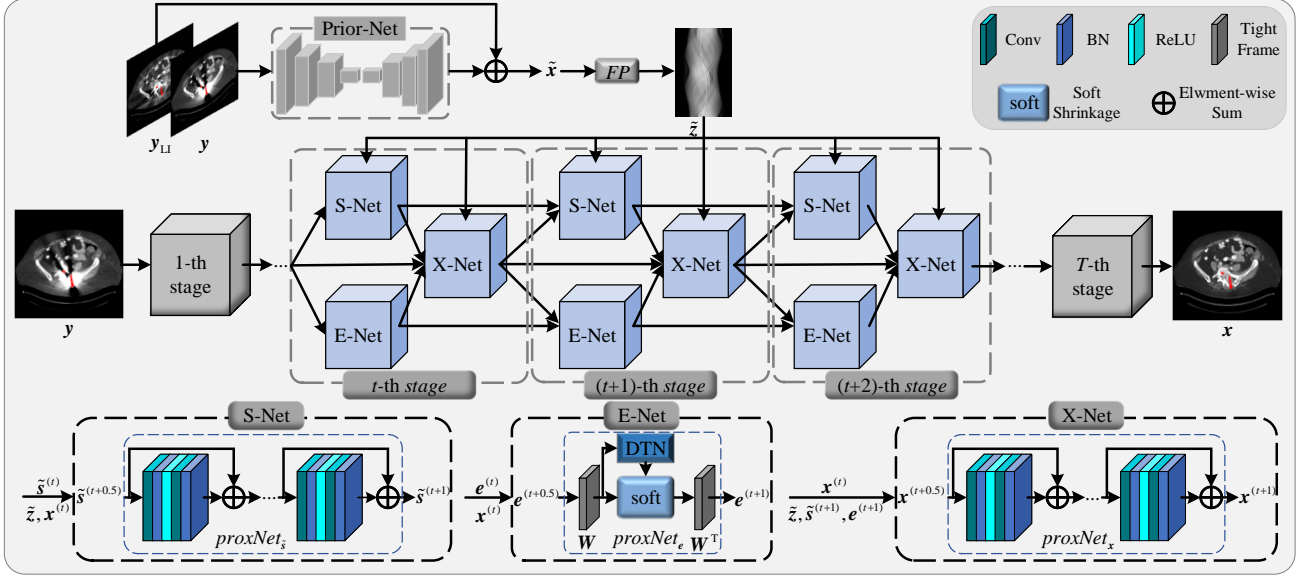


Fig. 1. The proposed TriDoNet architecture. The detailed structure at the $(t+1)$ -th stage where $\tilde{s}^{(t+1)}$, $e^{(t+1)}$, and $x^{(t+1)}$ are updated by S-Net, E-Net, and X-Net, respectively, based on Eqn. (8), Eqn. (11), and Eqn. (15). Specifically, S-Net and X-Net contain several residual blocks, and E-Net contains DTN to determine the thresholds. $proxNet_{\tilde{s}}$, $proxNet_e$, and $proxNet_x$ denote the proximal networks of the variables \tilde{s} , e , and x , respectively. The triple domain information is passed between and within each stage, enabling the features of triple domains to interact and promote each other.

where

$$\begin{aligned} x^{(t+0.5)} &= (1 - \eta_3) \mathbf{m} \odot x^{(t)} \\ &+ \eta_3 \mathbf{m} \odot (\mathbf{y} - e^{(t+1)}) - \alpha \eta_3 \mathbf{P}^T (\mathbf{P} x^{(t)} - \tilde{z} \odot \tilde{s}^{(t+1)}). \end{aligned} \quad (16)$$

B. Network architecture and loss function

In this section, we unroll the proposed iterative algorithm in Sec. II-A into a MAR network termed TriDoNet. As illustrated in Fig. 1, the proposed TriDoNet consists of T stages corresponding to T iterations of the iterative algorithm, and each stage contains S-Net, E-Net, and X-Net. The figure shows how the data flow within and between each stage, and this information interaction facilitates the reconstruction of favorable details in triple domains. Moreover, Prior-Net is utilized to produce the normalization coefficient \tilde{z} .

Prior-Net: The prior network in Fig. 1 is utilized to recover the preliminary corrected CT image \tilde{x} from the linear interpolation corrected CT image \mathbf{y}_{LI} and the metal-affected CT image \mathbf{y} . Then, the prior image \tilde{x} passes through the FP to obtain the prior sinogram \tilde{z} .

S-Net: At the $(t+1)$ -th stage, with \tilde{z} generated by Prior-Net, $\tilde{s}^{(t+0.5)}$ is obtained by Eqn. (9). We can get $\tilde{s}^{(t+1)} = proxNet_{\tilde{s}}(\tilde{s}^{(t+0.5)})$, where $proxNet_{\tilde{s}}(\bullet)$ consists of several [Conv+BN+ReLU+Conv+BN+Skip Connection] residual blocks.

E-Net: Given $\tilde{s}^{(t+1)}$ and $x^{(t+1)}$, $e^{(t+0.5)}$ is obtained and fed to $proxNet_e(\bullet)$ at the $(t+1)$ -th stage. The update rule of e is $e^{(t+1)} = proxNet_e(e^{(t+0.5)})$, where $proxNet_e(\bullet)$ is a tight frame network. To adaptively extract the thresholds from the inputs, we explore the DTN built by six convolution layers. Additionally, \mathbf{W} is learned by back-propagation in the training phase.

X-Net: Similarly, at the $(t+1)$ -th stage, given $\tilde{s}^{(t+1)}$, $e^{(t+1)}$, and \tilde{z} , the CT images can be updated by $x^{(t+1)} = proxNet_x(x^{(t+0.5)})$, where $proxNet_x(\bullet)$ consists of several [Conv+BN+ReLU+Conv+BN+Skip Connection] residual blocks.

Loss Function: To utilize triple domain knowledge, the triple domain loss function is designed to embed triple domain knowledge into the network training. With supervision on the sinogram $\tilde{s}^{(t)}$, the metal artifact $e^{(t)}$, and CT image $x^{(t)}$ at every stage, the triple domain loss function is defined as

$$\begin{aligned} L &= \omega_1 \|\mathbf{W}^T \mathbf{W} - \mathbf{I}\|_2^2 \\ &+ \sum_{t=0}^T \{ \omega_2 \|\mathbf{m} \odot (\mathbf{x} - x^{(t)})\|_2^2 + \omega_3 \|\mathbf{m} \odot (\mathbf{x} - x^{(t)})\|_1 \\ &+ \omega_4 \|\mathbf{m} \odot (\mathbf{y} - \mathbf{x} - e^{(t)})\|_1 + \omega_5 \|\tilde{z} \odot \tilde{s}^{(t)} - s_{gt}\|_2^2 \} \end{aligned} \quad (17)$$

where s_{gt} is the metal-free sinogram. The first term is the tight frame loss, the second and third terms are utilized for the image domain loss, the fourth term is the metal artifact domain loss, and the fifth term is the sinogram domain loss.

Inspired by contrastive learning [18], we fuse contrastive regularization to the triple domain loss to improve the quality of restored CT images. We define clean images \mathbf{x} as “positive” samples and metal-affected images \mathbf{y} as “negative” samples. We select common intermediate features from the same fixed pre-training model $G(\bullet)$ for the latent feature, e.g., VGG-19. Precisely, the formulated contrastive loss is defined as

$$CR(\mathbf{x}, x^{(T)}, \mathbf{y}) = \rho \sum_{i=1}^n \frac{\|G_i(x^{(T)}) - G_i(\mathbf{x})\|_1}{\|G_i(x^{(T)}) - G_i(\mathbf{y})\|_1} \quad (18)$$

TABLE I
QUANTITATIVE EVALUATIONS FOR DIFFERENT MAR METHODS ON DEEPLesion DATA. WE REPORT THE AVERAGE PSNR (dB)/SSIM VALUES OF THE TESTING DATASET FOR EACH CASE. THE BEST RESULTS ARE HIGHLIGHTED IN BOLD.

| Method | Large Metal | | | → | Small Metal | | Average |
|-----------|----------------|----------------|----------------|---|----------------|----------------|-----------------------|
| Input | 21.60 / 0.5442 | 24.72 / 0.6723 | 29.34 / 0.7185 | | 30.02 / 0.7541 | 31.60 / 0.7571 | 27.46 / 0.6892 |
| BHC | 24.57 / 0.6629 | 26.70 / 0.7327 | 29.80 / 0.7917 | | 30.26 / 0.8152 | 30.72 / 0.8183 | 28.41 / 0.7642 |
| LI | 31.30 / 0.9031 | 32.95 / 0.9295 | 36.41 / 0.9600 | | 37.46 / 0.9649 | 38.14 / 0.9723 | 35.20 / 0.9460 |
| NMAR | 31.75 / 0.9529 | 33.83 / 0.9484 | 36.91 / 0.9641 | | 37.65 / 0.9635 | 38.70 / 0.9782 | 35.77 / 0.9553 |
| CNNMAR | 33.19 / 0.9529 | 35.76 / 0.9700 | 38.69 / 0.9817 | | 39.13 / 0.9831 | 39.48 / 0.9855 | 37.25 / 0.9746 |
| DuDoNet | 33.52 / 0.9603 | 35.36 / 0.9708 | 40.49 / 0.9812 | | 42.04 / 0.9830 | 42.60 / 0.9841 | 38.80 / 0.9759 |
| InDuDoNet | 37.70 / 0.9708 | 38.83 / 0.9793 | 42.95 / 0.9858 | | 45.28 / 0.9877 | 45.50 / 0.9881 | 42.05 / 0.9824 |
| ACDNet | 37.82 / 0.9766 | 39.60 / 0.9828 | 43.85 / 0.9879 | | 45.46 / 0.9892 | 45.81 / 0.9896 | 42.51 / 0.9852 |
| TriDoNet | 40.71 / 0.9835 | 37.70 / 0.9837 | 44.09 / 0.9892 | | 46.55 / 0.9906 | 47.03 / 0.9911 | 43.22 / 0.9876 |

where G_i , $i = 1, 2, \dots, n$ extracts the i -th hidden features by using the fixed pre-trained VGG model, and ρ is a hyperparameter.

III. EXPERIMENTS AND RESULTS

Dataset: Following the simulation procedure in [4], [19], we select 1200 clean CT images from DeepLesion dataset [20] and 100 metal masks from [8] to synthesize metal artifacts at random. All CT images are resized to 416×416 . The size of the generated sinogram is 641×640 . We choose 1000 images and 90 metal masks for training and 10 metal masks together with 200 images for testing. The details of the experiment are provided in the supplementary material.

Performance Evaluation: To demonstrate the superiority of our TriDoNet, we compare the MAR performance of BHC [21], LI [5], NMAR [6], CNNMAR [8], DuDoNet [2], InDuDoNet [3], ACDNet [16], and the proposed TriDoNet. We employ peak signal-to-noise ratio (PSNR) and structural similarity index measure (SSIM) for quantitative evaluation. Table I summarizes the average PSNR and SSIM values on varying metal sizes. It can be observed that the proposed TriDoNet can achieve the highest average PSNR and SSIM values. Moreover, the average PSNR value of TriDoNet is nearly 0.71 dB and 1.17 dB higher than those of ACDNet and InDuDoNet, respectively. High-quality CT images restored by our TriDoNet are mainly attributed to the utilization of triple domain knowledge and the tight frame network. Figure 2 presents the MAR visual comparison. From the visual perspective, the proposed TriDoNet recovers evident tissue details finely and removes most metal artifacts.

Ablation Study: To demonstrate the effectiveness of TriDoNet, we compare the performance of different components. Under the same conditions, we compare single domain networks and dual domain networks for the MAR task. We remove CR to verify the effectiveness of contrastive learning and replace the threshold generated by DTN with a learnable parameter to demonstrate the effectiveness of the DTN. Table II shows that X-Net, S-Net, and E-net play their respective roles in processing each domain for the MAR task. Meanwhile, experiments demonstrate the effectiveness of CR and DTN in our model.

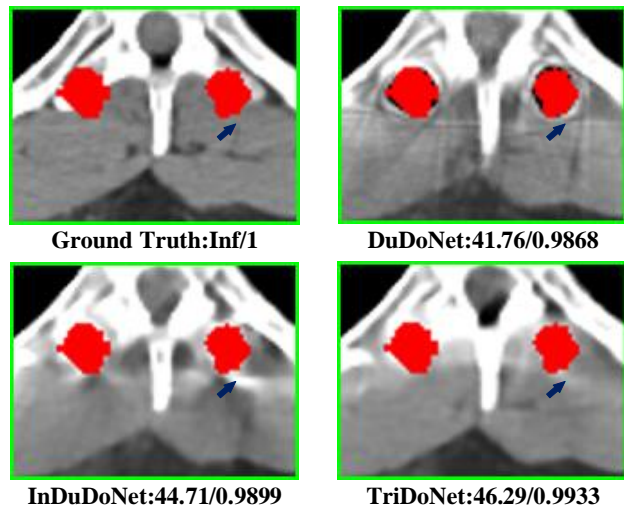


Fig. 2. Comparison for medium metallic implants from DeepLesion data. PSNR (dB)/SSIM is listed for reference. The red pixels stand for metallic implants. The window width is 450HU, and the window level is 50 HU.

TABLE II
AVERAGE PSNR (dB)/SSIM VALUES ACHIEVED BY TRI-DONET WITH DIFFERENT COMPONENTS ON SYNTHESIZED DATA. THE VARIATION REPRESENTS THE GAP WITH OUR ALGORITHM, AND THE BLUE ARROW INDICATES THE DECREASED VALUE.

| X-Net | S-Net | E-Net | CR | DTN | PSNR/SSIM | variation |
|-------|-------|-------|----|-----|--------------|--------------|
| × | ✓ | × | ✓ | ✓ | 37.73/0.8899 | ↓5.49/0.0977 |
| ✓ | × | × | ✓ | ✓ | 40.16/0.9797 | ↓3.06/0.0079 |
| ✓ | ✓ | × | ✓ | ✓ | 42.29/0.9847 | ↓0.93/0.0029 |
| ✓ | × | ✓ | ✓ | ✓ | 42.83/0.9868 | ↓0.39/0.0008 |
| ✓ | ✓ | ✓ | × | ✓ | 42.69/0.9872 | ↓0.53/0.0004 |
| ✓ | ✓ | ✓ | ✓ | × | 43.11/0.9858 | ↓0.11/0.0018 |
| ✓ | ✓ | ✓ | ✓ | ✓ | 43.22/0.9876 | 0/0 |

IV. CONCLUSION

In this paper, we embedded triple domain knowledge into a deep unfolding MAR framework and elaborated a tight frame network with adaptive thresholds to restore the metal artifacts. We also explored a contrastive loss to improve performance. Experiments show the effectiveness of the proposed triple domain model-driven MAR network.

REFERENCES

- [1] H. Wang, Y. X. Li, N. J. He, K. Ma, D. Y. Meng, and Y. F. Zheng, "DICDNet: Deep interpretable convolutional dictionary network for metal artifact reduction in CT images," *IEEE Transactions on Medical Imaging*, vol. 41, no. 4, pp. 869–880, April 2022.
- [2] W. -A. Lin, H. F. Liao, C. Peng, X. H. Sun, J. D. Zhang, J. B. Luo, R. Chellappa, and S. K. Zhou, "DuDoNet: Dual domain network for CT metal artifact reduction," in *Proceedings of the IEEE/CVF Conference on Computer Vision and Pattern Recognition (CVPR)*, June 2019, pp. 10504–10513.
- [3] H. Wang, Y. X. Li, H. M. Zhang, J. W. Chen, K. Ma, D. Y. Meng, and Y. F. Zheng, "InDuDoNet: An interpretable dual domain network for CT metal artifact reduction," in *Proceedings of International Conference on Medical Image Computing and Computer Assisted Intervention (MICCAI)*, September 2021, pp. 107–118.
- [4] L. Q. Yu, Z. C. Zhang, X. M. Li, and L. Xing, "Deep sinogram completion with image prior for metal artifact reduction in CT images," *IEEE Transactions on Medical Imaging*, vol. 40, no. 1, pp. 228–238, January 2021.
- [5] W. A. Kalender, R. Hebel, and J. Ebersberger, "Reduction of CT artifacts caused by metallic implants," *Radiology*, vol. 164, no. 2, pp. 576–577, August 1987.
- [6] E. Meyer, R. Raupach, M. Lell, B. Schmidt, and M. Kachelriess, "Normalized metal artifact reduction (NMAR) in computed tomography," *Medical physics*, vol. 37, no. 10, pp. 5482–5493, October 2010.
- [7] H. M. Zhang, B. Dong, and B. D. Liu, "A reweighted joint spatial-radon domain CT image reconstruction model for metal artifact reduction," *Society for Industrial and Applied Mathematics Journal on Imaging Sciences*, vol. 11, no. 1, pp. 707–733, March 2018.
- [8] Y. B. Zhang and H. Y. Yu, "Convolutional neural network based metal artifact reduction in X-ray computed tomography," *IEEE Transactions on Medical Imaging*, vol. 37, no. 6, pp. 1370–1381, June 2018.
- [9] M. U. Ghani and W. C. Karl, "Fast enhanced CT metal artifact reduction using data domain deep learning," *IEEE Transactions on Computational Imaging*, vol. 6, pp. 181–193, January 2020.
- [10] X. Huang, J. Wang, F. Tang, T. Zhong, and Y. Zhang, "Metal artifact reduction on cervical CT images by deep residual learning," *BioMedical Engineering OnLine*, vol. 17, no. 1, pp. 1–15, November 2018.
- [11] J. N. Wang, Y. Y. Zhao, J. H. Noble, and B. M. Dawant, "Conditional generative adversarial networks for metal artifact reduction in CT images of the ear," in *Proceedings of International Conference on Medical Image Computing and Computer Assisted Intervention (MICCAI)*, September 2018, pp. 3–11.
- [12] T. Wang, Z. X. Lu, Z. Y. Yang, W. J. Xia, M. Z. Hou, H. Q. Sun, Y. Liu, H. Chen, J. L. Zhou, and Y. Zhang, "IDOL-Net: An interactive dual-domain parallel network for CT metal artifact reduction," *IEEE Transactions on Radiation and Plasma Medical Sciences*, April 2022.
- [13] Z. Q. Chang, D. H. Ye, S. Srivastava, J. B. Thibault, K. Sauer, and C. Bouman, "Prior-guided metal artifact reduction for iterative X-ray computed tomography," *IEEE Transactions on Medical Imaging*, vol. 38, no. 6, pp. 1532–1542, June 2019.
- [14] Y. Y. Lyu, W. -A. Lin, H. F. Liao, J. J. Lu, and S. K. Zhou, "Encoding metal mask projection for metal artifact reduction in computed tomography," in *Proceedings of International Conference on Medical Image Computing and Computer Assisted Intervention (MICCAI)*, September 2020, pp. 147–157.
- [15] T. Wang, W. J. Xia, Y. Q. Huang, H. Q. Sun, Y. Liu, H. Chen, J. L. Zhou, and Y. Zhang, "Dual-domain adaptive-scaling non-local network for CT metal artifact reduction," in *Proceedings of International Conference on Medical Image Computing and Computer Assisted Intervention (MICCAI)*, September 2021, pp. 243–253.
- [16] H. Wang, Y. X. Li, D. Y. Meng, and Y. F. Zheng, "Adaptive convolutional dictionary network for CT metal artifact reduction," in *Proceedings of the Thirty-First International Joint Conference on Artificial Intelligence*, May 2022, pp. 1401–1407.
- [17] Y. Y. Lyu, J. J. Fu, C. Peng, and S. K. Zhou, "U-DuDoNet: Unpaired dual-domain network for CT metal artifact reduction," in *Proceedings of International Conference on Medical Image Computing and Computer Assisted Intervention (MICCAI)*, September 2021, pp. 296–306.
- [18] H. Y. Wu, Y. Y. Qu, S. H. Lin, J. Zhou, R. Z. Qiao, Z. Z. Zhang, Y. Xie, and L. Z. Ma, "Contrastive learning for compact single image dehazing," in *Proceedings of the IEEE/CVF Conference on Computer Vision and Pattern Recognition (CVPR)*, June 2021, pp. 10546–10555.
- [19] H. F. Liao, W. -A. Lin, S. K. Zhou, and J. Luo, "ADN: Artifact disentanglement network for unsupervised metal artifact reduction," *IEEE Transactions on Medical Imaging*, vol. 39, no. 3, pp. 634–643, March 2020.
- [20] K. Yan, X. S. Wang, L. Lu, L. Zhang, A. P. Harrison, M. Bagheri, and R. M. Summers, "Deep lesion graph in the wild: Relationship learning and organization of significant radiology image findings in a diverse large-scale lesion database," in *Proceedings of Deep Learning and Convolutional Neural Networks for Medical Imaging and Clinical Informatics*, September 2019, pp. 413–435.
- [21] J. M. Verburg and J. Seco, "CT metal artifact reduction method correcting for beam hardening and missing projections," *Physics in Medicine and Biology*, vol. 57, no. 9, pp. 2803–2818, April 2012.

I. TRAINING DETAILS

TriDoNet is implemented using PyTorch. We use the ADAM algorithm as the optimizer with $(\beta_1, \beta_2) = (0.5, 0.999)$ whose initial learning rate is 2×10^{-4} and decreased by a factor of 0.5 every 20 epochs. The model is trained on NVIDIA 3090Ti for 70 epochs. The parameters β , η_1 , η_2 , and η_3 are automatically learned from training samples in an end-to-end manner. Heuristically, the parameters are set to $\alpha = 1$, $\rho = 0.1$, μ_t ($t = 0, 1, \dots, T - 1$) = 0.1, and $\mu_T = 1$. Moreover, ω_1 , ω_2 , ω_3 , ω_4 , and ω_5 are hyperparameters to balance the weight of different loss items and we empirically set them to 0.001, μ_t , $5 \times 10^{-4}\mu_t$, $5 \times 10^{-4}\mu_t$, and $0.01\mu_t$, respectively.

On synthesized Deeplesion data, we select 200 CT images from 12 patients and 10 masks of different sizes to synthesize the test data. The dimensions of the metallic implants of the test data are: [2061, 890, 881, 451, 254, 124, 118, 112, 53, 35] in pixels. We compare TriDoNet with existing metal artifact reduction (MAR) methods, including BHC, LI, NMAR, CNNMAR, DuDoNet, InDuDoNet, and ACDNet. For the benchmark algorithms, we use the official codes, except for DuDoNet, we re-implement it since there is no official code.

II. MORE RESULTS

Figure 1 shows the visual comparison between our TriDoNet and the benchmark algorithms. For the convenience of observation, we enlarge the vicinity of metallic implants to display the recovery details. At the bottom of each image, we list the PSNR and SSIM values of the corresponding methods. In terms of visual quality, the images recovered by the InDuDoNet and ACDNet algorithms are blurring, and those achieved by the BHC, LI, NMAR, CNNMAR, and DuDoNet algorithms contain many artifacts. The images recovered by our proposed MAR method are better than those achieved by the benchmark MAR algorithms in terms of preserving details and reducing metal artifacts.

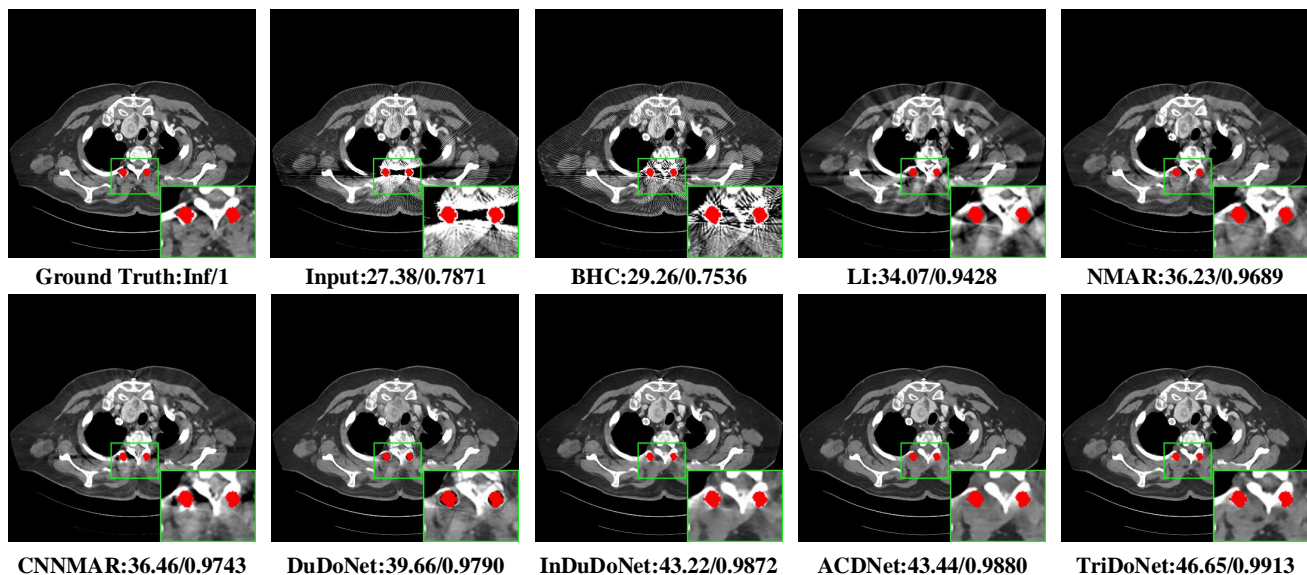


Fig. 1. Comparison for medium metallic implants from synthesized data. PSNR(dB)/SSIM is listed for reference. The magnified details are shown in the green boxes. Red pixels represent metallic implants. The window width is 450HU and the window level is 50 HU.